

000
001
002
003
004
005
006
007
008
009
010
011054
055
056
057
058
059
060
061
062
063
064
065
066
067
068
069
070
071
072
073
074
075
076
077
078
079
080
081
082
083
084
085
086
087
088
089
090
091
092
093
094
095
096
097
098
099
100
101
102
103
104
105
106
107

Graph-Based Neural Reconstruction from Morphological Skeletons

Anonymous CVPR submission

Paper ID 0446

Abstract

Advancements in electron microscopy image acquisition have created massive connectomics datasets in the terabyte range that make manual reconstruction of neuronal structures infeasible. Current state-of-the-art automatic methods segment neural membranes at the pixel level followed by agglomeration methods to create full neuron reconstructions. However, these approaches widely neglect global geometric properties that are inherent in the graph structure of neural wiring diagrams. In this work, we follow bottom-up pixel-based reconstruction by a top-down graph-based method to more accurately approximate neural pathways. Using the membrane labels of the pixel-based segmentation we first generate skeletons in 3D. Using this 3D graph we train automatic classifiers for shape description to detect impossible neural pathways by looking at geometric properties. We then apply efficient graph-based optimization strategies to improve the segmentation labels. We demonstrate the performance of our approach on multiple real-world connectomics datasets with an average variation of information improvement of $X \times$.

1. Introduction

The field of connectomics is concerned with reconstructing the wiring diagram of the brain at nanometer resolutions to enable new insights into the workings of the brain [8, 16]. Recent advancements in image acquisition using multi-beam serial-section electron microscopy (sSEM) have allowed researchers to produce terabytes of image data every hour [11]. It is not feasible for domain experts to manually reconstruct thousands or millions of neurons from this vast amount of image data [10]. State-of-the-art automatic reconstruction approaches use pixel-based segmentation with convolutional neural networks (CNNs) followed by agglomeration strategies [19, 20, 24, 27, 30, 41]. These bottom-up pixel-based algorithms produce excellent results but still fall short of acceptable error rates for large volumes.

We present a *top-down graph-based* method that builds on the outputs of bottom-up pixel-based segmentation ap-

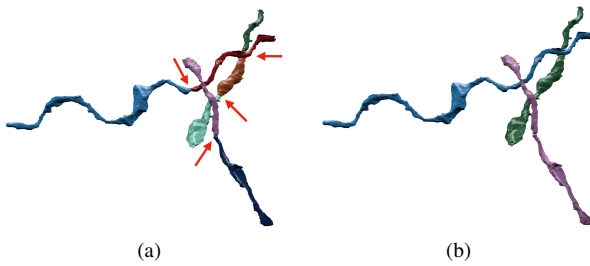


Figure 1: Example improvement of neural reconstruction. (a) We extract 3D skeletons from pixel-based segmentation algorithms to create a graph representation with error probabilities indicated by the red arrows. (b) We then improve the accuracy of segmentation labels using graph partitioning algorithms with local and global geometric features.

proaches. We first extract 3D skeletons from the input segmentation (Fig. 2) and generate a simplified 3D graph (Fig. 1a). We train a 3D CNN classifier on the agglomerated regions in the segmentation data to detect errors. During test time, we run the classifier to populate the graph edge weights with error probabilities. We then use a graph optimization algorithm to partition the graph into the final reconstruction by enforcing domain-specific global constraints from the underlying biology (Fig. 1b).

Our approach operates at a level of abstraction above existing pixel-based methods. This allows us to leverage both local and global information to produce more accurate reconstructions. Since it uses agglomerated regions, our classifier is independent of image resolution and acquisition parameters, enabling its application to isotropic and anisotropic image data without retraining. Using the 3D graph of the segmentation allows us to enforce global constraints on the reconstruction that closely follow the underlying biology. We can also use local information such as shape priors to weight the edges in our graph. This dual approach of assessing local decisions in a global context yields accuracy improvements over the existing reconstruction methods.

This work makes the following following contributions:

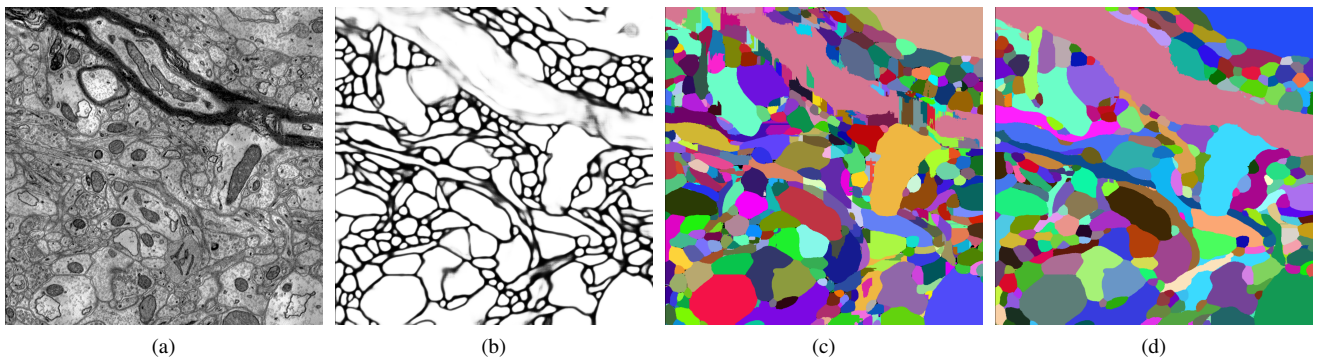
108
109
110
111
112
113
114
115
116
117
118
119
120121
122
123
124
125
126
127
128
129
130
131
132
133
134
135
136
137
138
139
140
141
142
143
144
145
146
147
148
149
150
151
152
153
154
155
156
157
158
159
160
161

Figure 2: An overview of a pixel-based connectomics segmentation pipeline. (a) Original EM image data (b) Output of a CNN predicting voxel affinities (c) Clustering of the affinities using a watershed algorithm (d) Agglomeration of the super-voxels into larger segments.

(1) a novel top-down graph-based method for neural reconstruction of connectomics data; (2) a region-based CNN classifier to detect errors under global constraints; (3) an empirical evaluation of our method on several connectomics datasets; (4) our method yields improved performance over the state-of-the-art on three testing datasets. On average, we improve the Variation of Information (VI) metric across all datasets by $\textcolor{red}{X}$ percent without drastically increasing the running time.

2. Related Work

A significant amount of research in computer vision focuses on the segmentation of images [39]. Here, we review some of the most successful methods that have been applied to large-scale EM images in connectomics. Fig. 2 shows the results of a typical connectomics segmentation pipeline.

Pixel-based methods. A large amount of connectomics research considers the problem of extracting segmentation information at the pixel (i.e., voxel) level from the raw EM images. Some early techniques apply computationally expensive graph partitioning algorithms with a single node per pixel [1]. However these methods do not scale to terabyte datasets. More recent methods train classifiers to predict membrane probabilities per image slice either using 2D [4, 13, 17, 19, 38] or 3D CNNs [20, 30, 37].

Oftentimes these networks produce probabilities for the affinity between two voxels (i.e., the probability that adjacent voxels belong to the same neuron). The MALIS cost function is specifically designed for generating affinities that produce good segmentations [2]. More recently, flood-filling networks produce segmentations by training an end-to-end neural network that goes from EM images directly to label volumes [14]. These networks produce impressive accuracies but at a high computational cost.

162
163
164
165
166
167
168
169
170
171
172
173
174
175
176
177
178
179
180
181
182
183
184
185
186
187
188
189
190
191
192
193
194
195
196
197
198
199
200
201
202
203
204
205
206
207
208
209
210
211
212
213
214
215

Region-based methods. Several pixel-based approaches generate probabilities that neighboring pixels belong to the same neuron. Often a watershed algorithm will cluster pixels into small super-pixels [41]. Many methods build on top of these strategies and train random-forest classifiers to produce region-based (i.e., super-pixel) segmentations [19, 24, 26, 27, 41].

Segment-based methods. Some recent research builds on top of these region-based methods to correct errors in the segmentation [29, 42, 9]. However, to our knowledge, our method is the first to extract a 3D graph from pixel-based agglomerated segmentations for a true top-down reconstruction approach. This allows us to enforce domain-specific constraints using graph-based partitioning algorithms. Many segmentation and clustering algorithms use graph partitioning techniques [1] or normalized cuts for traditional image segmentation [15, 33, 35]. Even though graph partitioning is an NP-Hard problem [5] there are several useful multicut heuristics that provide good approximations with reasonable computational costs [12]. We use the method of Keuper et al. to partition the extracted 3D graph into the final neuron reconstruction [18].

3. Method

There are two types of errors that can occur in connectomics segmentation. The first, called a split error, occurs when there are two segments that should have been merged. The second, called a merge error, happens when one segment should be split into two. Generally, it is much more difficult to correct merge errors than to correct split errors, as the space of possible split proposals grow quickly [25]. Thus, most reconstruction approaches are tuned towards over-segmentation with many more split than merge errors. Our method takes as input over-segmentations of EM image

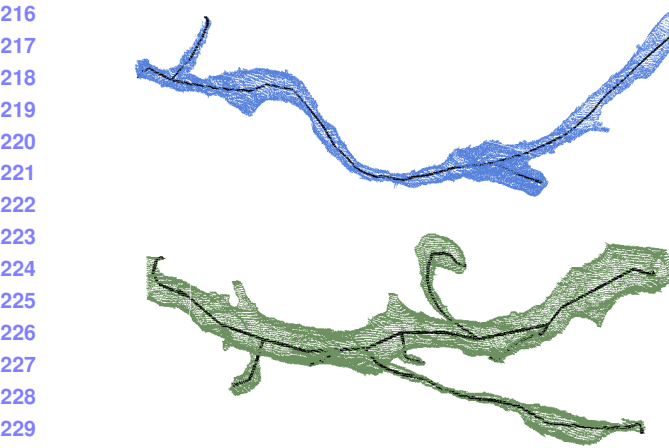


Figure 3: Example skeletons (in black) extracted from segments (blue and green) using the TEASER algorithm.

volumes generated by state-of-the-art connectomics reconstruction pipelines (Sec. 4.2). Our goal is to identify locations of split errors and merge the corresponding segments automatically.

From the input segmentation we generate a graph G with nodes N and edges E with non-negative edge weights w_e . The nodes correspond to label segments from the segmentation with edges between segments considered for merging. Ideally, our graph has edges corresponding to all of the segments that were erroneously split. To compute this graph we generate a skeleton for every segment in the pixel-based segmentation. The skeleton is a simplified representation of the overall shape of the neurons. From this skeleton we identify potential merge locations and produce the corresponding edges for the graph. To find actual merges we run a classification CNN to generate edge weights that correspond to probabilities of merging. We then use a multicut heuristic to generate a partition on the graph where nodes in the same partition are assigned the same output label in the improved segmentation. We will now discuss the three major components to our framework (graph creation, edge weights assignment, and graph partitioning) in more detail.

3.1. Node Generation

The simplest node generation strategy creates one node for every unique segment label in the input volume. However, some of the millions of labels in the volume correspond to very small structures that are likely the result of segmentation errors. This typically happens in regions with noisy image data such that pixel-based methods could not generate the correct segments. It is difficult to extract useful shape features from these segments because of their small, and often random, shape. We prune these nodes from the graph by removing all segments with fewer than a thresh-

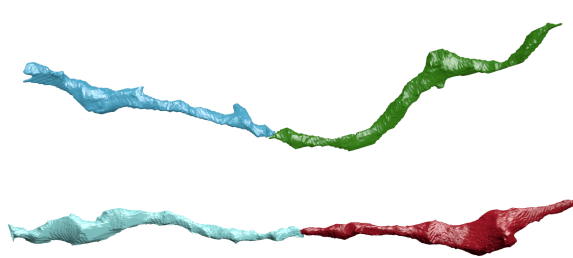


Figure 4: Two erroneously split segments.

old of t_{seg} voxels. We use $t_{seg} = 20,000$ voxels, which removed on average 56% of the segments in our datasets (Sec. 4.1). Despite the large number of segments, these regions only take up 1.6% of the total volume on average.

3.2. Edge Generation

A typical approach to generating edges produces an edge between all adjacent segments. Two segments l_1 and l_2 are considered adjacent if there is a pair of adjacent voxels where one has label l_1 and the other has label l_2 . For example, pixel-based agglomeration methods such as NeuroProof [26] and GALA [24] consider all pairs of adjacent segments for merging. However, this method produces too many edges in the graph for graph-based optimization approaches. We identify a smaller number of pairs of segments to consider as graph edges using the following algorithm.

First, we extract a skeleton from each segment using the TEASER algorithm [31, 40]. Fig. 3 shows an example of two extracted skeletons (in black) of two segments from the label volume. These skeletons consist of a sequence of *joints*, i.e., locations that are a local maximum distance from the segment boundary, with line segments connecting successive joints. We prune the joints that are within $t_{jnt} = 50$ voxels of each other to reduce unnecessary branching. For the purposes of our algorithm, joints that have only one connected neighbor are referred to as *endpoints*. Many of the segments that are erroneously split have nearby endpoints (Fig. 4). We make use of this fact to merge segments with the following two-pass heuristic.

In the first pass, we iterate over all endpoints e belonging to a segment S and create a set of segments \mathbb{S}'_e that includes all labels that are within t_{low} voxels from e . Elements of \mathbb{S}'_e are candidates for merging. However, this first pass often leads to too many candidates, requiring an additional pass for further pruning. In the second pass, we consider all of the segments in \mathbb{S}'_e for every endpoint e . If a segment $S' \in \mathbb{S}'_e$ has an endpoint within t_{high} voxels of e , the segment S and S' are considered for merging. We store the midpoints between the two endpoints as the center of the potential merges in the set \mathbb{S}_c .

324

3.3. Edge Weights Assignment

We assign non-negative edge weights w_e to each edge where the weight corresponds to the probability two nodes belong to the same neuron. Instead of using handcrafted features to compute the similarity between adjacent nodes, we train a 3D CNN classifier to learn from the manually labeled oversegmentation input volume (Sec. 4.1).

325

326

327

328

329

330

331

332

333

334

335

336

337

338

339

340

341

342

343

344

345

346

347

348

349

350

351

352

353

354

355

356

357

358

359

360

361

362

363

364

365

366

367

368

369

370

371

372

373

374

375

376

377

3.3.1 Classifier Input

We extract a cubic region of interest around each endpoint e in \mathbb{S}_c as input to the CNN. These regions of interest provide the local information for the neural network to predict which neighboring segments belong to the same neuron. The CNN receives three input channels for every voxel in the region of interest around segments l_1 and l_2 . The input in all of the channels is in the range $\{-0.5, 0.5\}$. The first channel is 0.5 only if the corresponding voxel has label l_1 . The second channel is 0.5 only if the corresponding voxel has label l_2 . The third channel is 0.5 if the corresponding voxel is either l_1 or l_2 .

378

379

380

381

382

383

384

385

386

387

388

389

390

391

392

393

394

395

396

397

398

399

400

401

402

403

404

405

406

407

408

409

410

411

412

413

414

415

416

417

418

419

420

421

422

423

424

425

426

427

428

429

430

431

3.3.2 Network Architecture & Training

Fig. 5 provides an overview of our CNN architecture. Similar to Chatfield et al. [3] it consists of three layers of double convolutions followed by a max pooling step. The first max pooling layer is anisotropic with pooling only in the x and y dimensions. The output of this final pooling step is flattened into a 1D vector that is input into two fully connected layers. The final layer produces probabilities with a sigmoid activation function [6]. All of the other activation functions are LeakyReLU [21].

We use a stochastic gradient descent optimizer with Nesterov’s accelerated gradient [23] for training. We employ dropouts of 0.2 after every pooling layer and the first dense layer, and a dropout of 0.5 after the final dense layer to prevent overfitting. We discuss all other network parameters in Sec. 4.4.

364

365

366

367

368

369

370

371

372

373

374

375

376

377

3.4. Graph Partitioning

After constructing the 3D graph we apply graph-based partitioning to compute the final segmentation. Using graph partitioning from the top down allows us to apply biological constraints on the output. Neuroscientists know that neuronal connectivity graphs in the brain are acyclic (i.e., the graphs have a genus of zero). We enforce this constraint by finding a multicut partition of the graph that generates a *forest* of nodes. A forest is a partitioning of a graph into a set of trees where no segment has a cycle. To solve this constrained multicut problem we use the method by Keuper et al. [18] that produces a feasible solution by greedy additive edge contraction. Adding additional constraints and

improving the graph partition algorithm are areas for future work.

378

379

380

381

382

383

384

385

386

387

388

389

390

391

392

393

394

395

396

397

398

399

400

401

402

403

404

405

406

407

408

409

410

411

412

413

414

415

416

417

418

419

420

421

422

423

424

425

426

427

428

429

4. Experimental Results

We evaluate our method on two connectomics datasets and compare it to a state-of-the-art pixel-based reconstruction method using the variation of information (VI) metric.

HP: depending on space we can shorten this and put details into the supplemental material

4.1. Datasets

We use the following two datasets for training and experimental evaluation.

Kasthuri. The Kasthuri dataset consists of scanning electron microscope images of the neocortex of a mouse brain [16]. This dataset is $5342 \times 3618 \times 338$ voxels in size. The resolution of the dataset is $3 \times 3 \times 30 \text{ nm}^3$ per voxel. We evaluate our methods using the left cylinder of this 3-cylinder dataset. We downsample the dataset in the x and y dimensions to give a final resolution of $6 \times 6 \times 30 \text{ nm}^3$ per voxel. We divide the dataset into two volumes (Vol. 1 and Vol. 2) along the x dimension where each volume is $8.0 \times 10.9 \times 10.1 \mu\text{m}^3$.

FlyEM. The FlyEM dataset comes from the mushroom body of a 5-day old adult male *Drosophila* fly imaged by a focused ion-beam milling scanning electron microscopy [34]. The mushroom body in this species is the major site of associative learning. The original dataset contains a $40 \times 50 \times 120 \mu\text{m}^3$ volume of which we use two cubes of size $10 \times 10 \times 10 \mu\text{m}^3$. The resolution of this dataset is $10 \times 10 \times 10 \text{ nm}^3$ or 1000 voxels in each dimension in each of the two volumes.

4.2. Pixel-Based Segmentations

The segmentation on the Kasthuri dataset was computed by agglomerating 3D supervoxels produced by the z-watershed algorithm from 3D affinity predictions [41]. A recent study by Funke et al. [32] demonstrated superior performance of such methods over existing ones on anisotropic data. We learn 3D affinities using MALIS loss with a U-net [36, 30]. We apply the z-watershed algorithm with suitable parameters to compute a 3D oversegmentation of the volume. The resulting 3D oversegmentation is then agglomerated using the technique of context-aware delayed agglomeration to generate the final segmentation [26]. We use this segmentation as our baseline for comparisons with our method.

For the FlyEM data we collected two $1000 \times 1000 \times 1000$ voxel ($10 \times 10 \times 10 \mu\text{m}^3$) volumes from the authors [34].

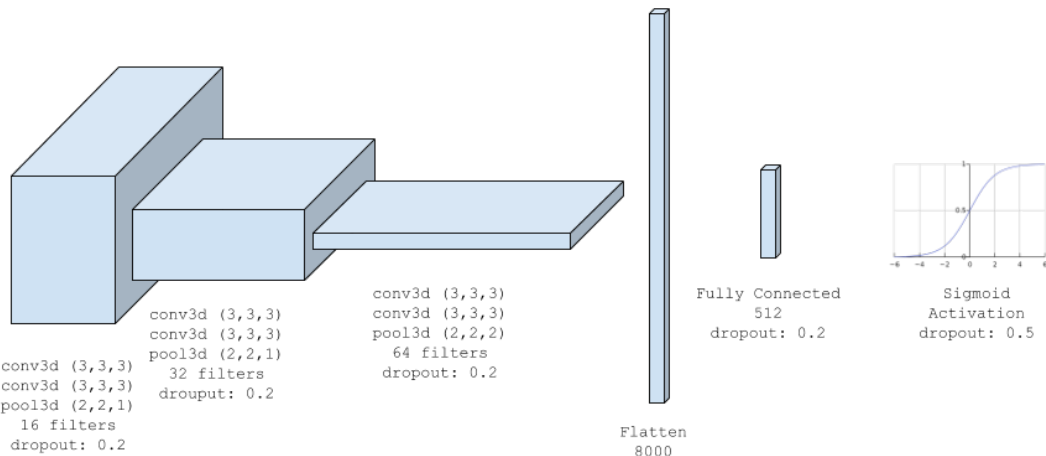


Figure 5: The architecture for our classification CNN uses double convolutions followed by max pooling. The number of filters doubles each layer, with a final fully connected layer and sigmoid activation function.

Based on the authors' suggestion, we applied a context-aware delayed agglomeration algorithm [26] that shows improved performance on this dataset over the pipeline used in the original publication. This segmentation framework learns voxel and supervoxel classifiers with an emphasis to minimize under-segmentation error. At the same time this framework produces lower oversegmentation than standard algorithms. The algorithm first computes multi-channel 3-D predictions for membranes, cell interiors, and mitochondria, among other cell features. The membrane prediction channel is used to produce an over-segmented volume using 3D watershed, which is then agglomerated hierarchically up to a certain confidence threshold. We used exactly the same parameters as the publicly available code for this algorithm.

4.3. Graph Generation Parameters

There are two essential parameters to the graph generation algorithm described in Section 3.1: t_{low} and t_{high} . Ideally, the merge candidates output by this algorithm will contain all possible positive examples with a very limited number of negative examples. After considering various thresholds, we find that $t_{low} = 240$ nm and $t_{high} = 600$ nm produce the best results considering this objective.

In our implementation we use nanometers for these thresholds and not voxels. Connectomics datasets often have lower sample resolutions in z . Using nanometers allows us to have uniform units across all of these datasets and calculate the thresholds in voxels at runtime. For example, the thresholds in voxels are $t_{low} = (40, 40, 8)$ and $t_{high} = (100, 100, 20)$ for the anisotropic Kasthuri dataset and $t_{low} = (24, 24, 24)$ and $t_{high} = (60, 60, 60)$ for the isotropic FlyEM dataset.

4.4. Classifier Training

We use the left cylinder of the Kasthuri dataset for training and validation. We train on 80% of the potential merge candidates for this volume. We validate the CNN classifier on the remaining 20% of candidates. We apply data augmentation to the generated examples to increase the size of the training datasets. We consider all rotations of 90 degrees along the xy -plane in addition to mirroring along the x and z axes. This produces 16 times more training data.

We consider networks with varying input sizes, optimizers, loss functions, filter sizes, learning rates, and activation functions. The supplemental material includes information on the experiments that determined these final parameters. Table 1 provides the parameters of the final network. There are 7,294,705 learnable parameters in our final architecture. All the parameters are randomly initialized following the Xavier uniform distribution [7]. Training concluded after 34 epochs.

Parameters	Values
Loss Function	Mean Squared Error
Optimizer	SGD with Nesterov Momentum
Momentum	0.9
Initial Learning Rate	0.01
Decay Rate	$5 * 10^{-8}$
Activation	LeakyReLU ($\alpha = 0.001$)
Kernel Sizes	$3 \times 3 \times 3$
Filter Sizes	$16 \rightarrow 32 \rightarrow 64$

Table 1: Training parameters.

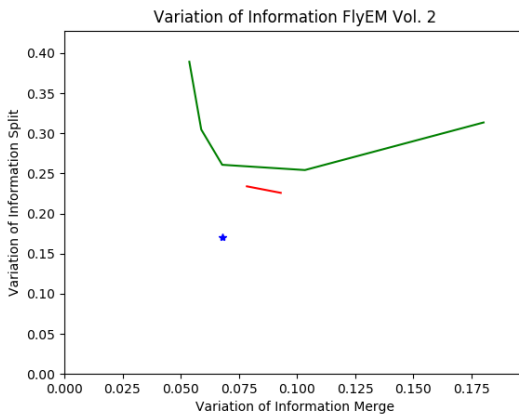
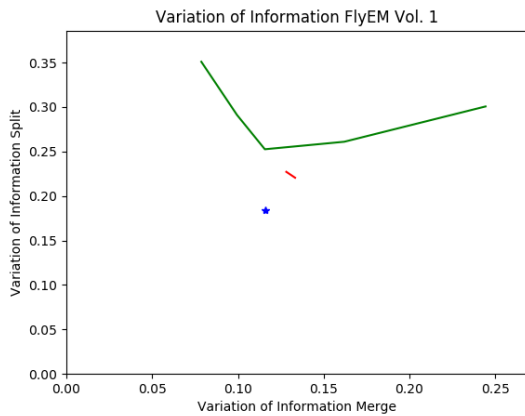
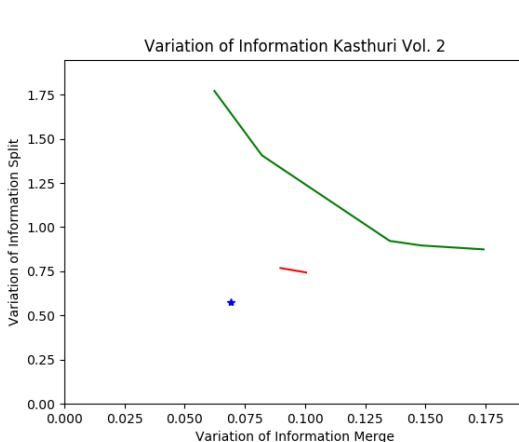
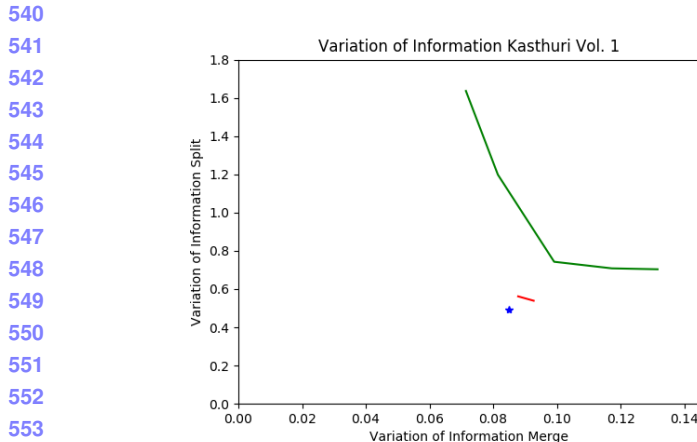


Figure 6: VI scores of our method (red) compared to the baseline segmentation (green) and an oracle (blue) that optimally partitions the graph based on ground truth.

5. Results

5.1. Error Metric

We evaluate the performance of the different methods using the split version of variance of information (VI) [22]. Given a ground truth labeling GT and our automatically reconstructed segmentation SG , over and undersegmentation are quantified by the conditional entropy $H(GT|SG)$ and $H(SG|GT)$, respectively. Since we are measuring the entropy between two clusterings, better VI scores are closer to the origin.

5.2. Variation of Information Improvement

In Fig. 6, we show the VI results of NeuroProof on the Kasthuri and FlyEM data at varying thresholds of agglomeration (green). The green circle represents the variation of information for our input segmentation (a threshold of 0.3 for all datasets). Our results are in red. We show the comparison to an oracle (blue) that correctly partitions the graph from our algorithm based on ground truth.

Our algorithm improves the accuracy of the input seg-

mentation on every dataset, reducing the VI split score on average by X% and only increasing the VI merge score by X%. Scores closer to the origin are better for this metric, and in every instance we are below the green curve. We see significant improvements on the Kasthuri datasets (VI split reduction of X% and X% on the training and testing datasets respectively) and slightly more modest improvements on the FlyEM datasets (reduction of X% and X%). However, our baseline, NeuroProof performs much better on the FlyEM datasets reducing the potential improvement. Isotropic datasets are easier to segment using state-of-the-art region-based methods than anisotropic ones [28]. Thus there is less room for improvement on these datasets.

Fig. 7 shows successful merges on the Kasthuri Vol. 2 dataset. Several of these examples combine multiple consecutive segments that span the volume. In the third example we correct the oversegmentation of a dendrite. Fig. 8 shows some failure cases. In two of these examples the algorithm correctly predicted several merges but made one error. In the third example a merge error in the initial segmentation propagated to our output. We now analyze how

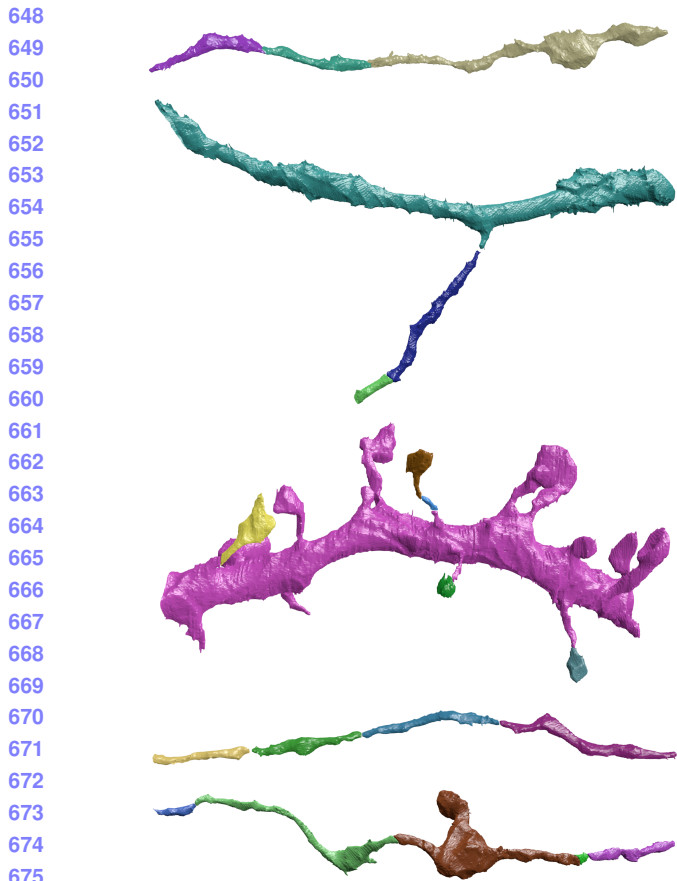


Figure 7: Correctly segmented neurons from our method.

Dataset	Baseline	After Pruning
Kasthuri Vol. 1	763 / 21242 (3.47%)	753 / 3459 (17.88%)
Kasthuri Vol. 2	1010 / 26073 (3.73%)	904 / 4327 (17.28%)
FlyEM Vol. 1	269 / 14875 (1.78%)	262 / 946 (21.69%)
FlyEM Vol. 2	270 / 16808 (1.58%)	285 / 768 (27.07%)

Table 2: The results of our skeleton graph pruning heuristic compared to the baseline segmentation.

each major component of our method contributes to this final result.

5.3. Graph Creation

Table 2 shows the results of pruning the skeleton graph using the heuristic discussed in Sec. 3.1. The baseline algorithm considers all adjacent regions for merging. Our method removes a significant portion of these candidates while maintaining a large number of the true merge locations. This edge pruning is essential for the graph partitioning algorithm, which has a computational complexity dependence on the number of edges. Our pruning heuristic removes at least $6 \times$ the number of edges between cor-

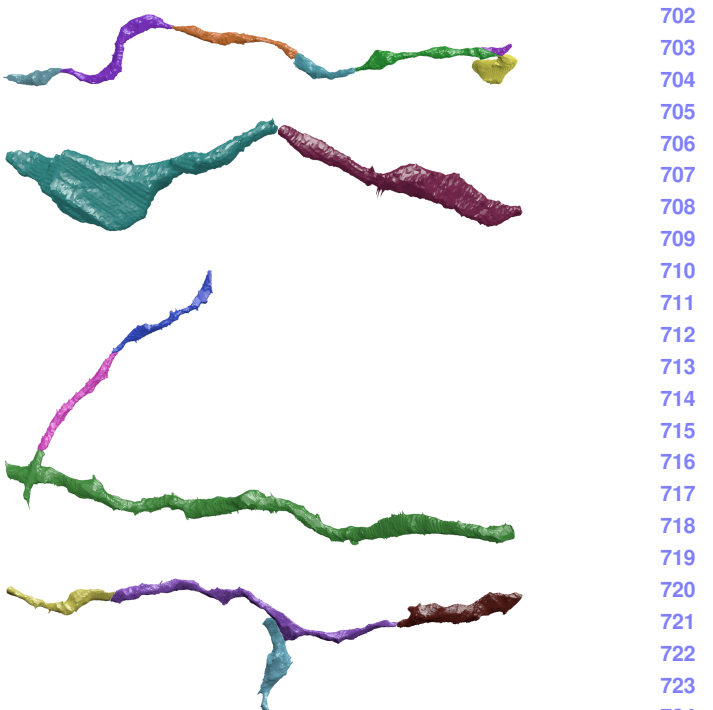


Figure 8: Errors made by our method.

rectly split segments on all datasets, achieving a maximum removal ratio of $20 \times$.

Equally important is the number of split errors that remain after pruning. These are the locations that we want to merge to create a more accurate reconstruction. For every dataset, the number of true split errors remains constant before and after pruning. However, since our heuristic does not enforce an adjacency constraint of two regions when constructing edges in the graph, the difference does not indicate the number of examples excluded by pruning. In fact, our method finds a number of examples that are non-adjacent. Figure 9 shows two example segments with split errors, one that our algorithm missed (top) and one that it identified (bottom), despite the fact that the split segments are not adjacent. Of the successful examples in Figure 7, the second and fourth groupings contain pairs of non-adjacent segments that merge with our algorithm.

5.4. Classification Performance

Figure 10 shows the receiver operating characteristic (ROC) curve for all of the datasets. We train our CNN using one of the Kasthuri volumes and test using the other three datasets. Since our CNN only takes as input a region of the label volume we can train on an anisotropic dataset and infer on an isotropic one. This provides a major benefit given the time-intensive task of manually generating ground truth data at various resolutions.



Figure 9: Example merge candidates.

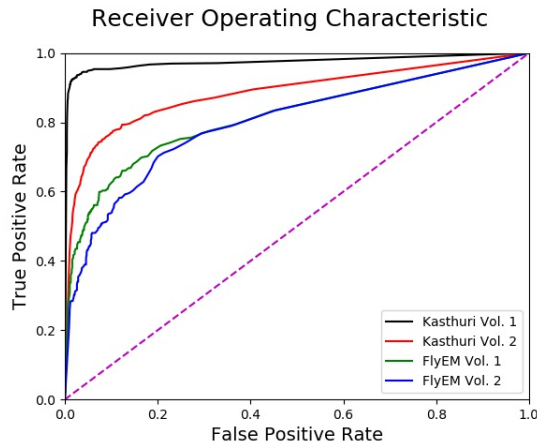


Figure 10: The receiver operating characteristic for all four datasets.

As evidenced by the ROC curve, the test results on the Kasthuri data are better than the results for FlyEM. We believe this is in part because of the differences in the datasets (i.e., isotropy and xy resolution). To test this hypothesis, we also evaluate the performance of the FlyEM datasets when the network trains on FlyEM Vol. 1 and infers on FlyEM Vol. 2.¹ The dotted lines in the figure represent these tests. There is a slight performance increase for FlyEM Vol. 2. However, the FlyEM datasets have reasonable results when the network is trained by the Kasthuri data, and the results outside of this section follow from that setup.

5.5. Graph Based Strategies

The graph-based optimization strategy increases our correction accuracy over using just the CNN. In particular, the precision increases on each dataset, although the recall decreases on all but one of the datasets. Since it is more difficult to correct merge errors than split errors, it is often desirable to sacrifice recall for precision. Table 3 shows the changes in precision, recall, and accuracy for

¹Since the FlyEM datasets have significantly fewer examples, we initialize the network with the weights from the Kasthuri training and have an initial learning rate of 10^{-4} .

all four datasets compared to the CNN. Over the three testing datasets, applying a graph-based partitioning strategy reduced the number of merge errors by X, Y, and Z.

Dataset	Δ Precision	Δ Recall	Δ Accuracy
Kasthuri Training	+3.60%	-0.01%	+0.60%
Kasthuri Testing	+7.59%	-1.77%	+1.38%
FlyEM Vol. 1	+2.68%	+0.76%	+0.66%
FlyEM Vol. 2	+2.22%	-1.05%	+0.29%

Table 3: Precision and recall for the training and three test datasets.

6. Conclusions

We present a novel method for reconstructing neuronal processes in connectomics datasets. We extend existing region-based reconstruction strategies using a morphological 3D skeleton graph and show significant accuracy improvement on two datasets from two different species. Our approach enables enforcing domain-constraints on the resulting segmentation. We believe this approach extends beyond connectomics to other domains with different constraints.

There is significant room for additional research related to this topic. We can still extract a lot more information from the skeletons of each segment. Currently these skeletons identify potential merge locations. However, these representations can be used to identify improperly merged segments. Additionally, we can further improve our results by tweaking the partitioning cost functions to more closely match the underlying biology. One such extension might take the outputs of a synaptic detector to enforce the constraint that a given segment only has post- or pre-synaptic connections.

References

- [1] B. Andres, T. Kroeger, K. L. Briggman, W. Denk, N. Korogod, G. Knott, U. Koethe, and F. A. Hamprecht. Globally optimal closed-surface segmentation for connectomics. In *European Conference on Computer Vision*, pages 778–791. Springer, 2012. 2
- [2] K. Briggman, W. Denk, S. Seung, M. N. Helmstaedter, and S. C. Turaga. Maximin affinity learning of image segmentation. In *Advances in Neural Information Processing Systems*, pages 1865–1873, 2009. 2
- [3] K. Chatfield, K. Simonyan, A. Vedaldi, and A. Zisserman. Return of the devil in the details: Delving deep into convolutional nets. *arXiv preprint arXiv:1405.3531*, 2014. 4
- [4] D. Ciresan, A. Giusti, L. M. Gambardella, and J. Schmidhuber. Deep neural networks segment neuronal membranes in electron microscopy images. In *Advances in neural information processing systems*, pages 2843–2851, 2012. 2

- 864 [5] E. D. Demaine, D. Emanuel, A. Fiat, and N. Immorlica. Cor- 918
 865 relation clustering in general weighted graphs. *Theoretical 919
 866 Computer Science*, 361(2-3):172–187, 2006. 2 920
 867 [6] K.-I. Funahashi. On the approximate realization of con- 921
 868 tinuous mappings by neural networks. *Neural networks*, 922
 869 2(3):183–192, 1989. 4 923
 870 [7] X. Glorot and Y. Bengio. Understanding the difficulty of 924
 871 training deep feedforward neural networks. In *Proceedings 925
 872 of the Thirteenth International Conference on Artificial 926
 873 Intelligence and Statistics*, pages 249–256, 2010. 5 927
 874 [8] D. Haehn, J. Hoffer, B. Matejek, A. Suissa-Peleg, A. K. 928
 875 Al-Awami, L. Kamentsky, F. Gonda, E. Meng, W. Zhang, 929
 876 R. Schalek, et al. Scalable interactive visualization for 930
 877 connectomics. In *Informatics*, volume 4, page 29. Multidisciplinary 931
 878 Digital Publishing Institute, 2017. 1 932
 879 [9] D. Haehn, V. Kaynig, J. Tompkin, J. W. Lichtman, and 933
 880 H. Pfister. Guided proofreading of automatic segmentations 934
 881 for connectomics. *arXiv preprint arXiv:1704.00848*, 2017. 935
 882 2
 883 [10] D. Haehn, S. Knowles-Barley, M. Roberts, J. Beyer, 936
 884 N. Kasthuri, J. W. Lichtman, and H. Pfister. Design and eval- 937
 885 uation of interactive proofreading tools for connectomics. 938
 886 *IEEE Transactions on Visualization and Computer Graph- 939
 887 ics*, 20(12):2466–2475, 2014. 1
 888 [11] D. G. C. Hildebrand, M. Cicconet, R. M. Torres, W. Choi, 940
 889 T. M. Quan, J. Moon, A. W. Wetzel, A. S. Champion, B. J. 941
 890 Graham, O. Randlett, et al. Whole-brain serial-section elec- 942
 891 tron microscopy in larval zebrafish. *Nature*, 545(7654):345– 943
 892 349, 2017. 1 944
 893 [12] A. Horňáková, J.-H. Lange, and B. Andres. Analysis and 945
 894 optimization of graph decompositions by lifted multicut. In *946
 895 International Conference on Machine Learning*, pages 1539– 947
 896 1548, 2017. 2 948
 897 [13] V. Jain, B. Bollmann, M. Richardson, D. Berger, 949
 898 M. Helmstädtter, K. Briggman, W. Denk, J. Bowden, 950
 899 J. Mendenhall, W. Abraham, K. Harris, N. Kasthuri, K. Hay- 951
 900 worth, R. Schalek, J. Tapia, J. Lichtman, and S. Seung. 952
 901 Boundary learning by optimization with topological 953
 902 constraints. In *Proc. IEEE CVPR 2010*, pages 2488–2495, 2010. 954
 903 2
 904 [14] M. Januszewski, J. Maitin-Shepard, P. Li, J. Kornfeld, 955
 905 W. Denk, and V. Jain. Flood-filling networks. *arXiv preprint 956
 906 arXiv:1611.00421*, 2016. 2
 907 [15] J. H. Kappes, M. Speth, G. Reinelt, and C. Schnörr. Higher- 957
 908 order segmentation via multicut. *Computer Vision and 958
 909 Image Understanding*, 143:104–119, 2016. 2
 910 [16] N. Kasthuri, K. J. Hayworth, D. R. Berger, R. L. Schalek, 959
 911 J. A. Conchello, S. Knowles-Barley, D. Lee, A. Vázquez- 960
 912 Reina, V. Kaynig, T. R. Jones, et al. Saturated reconstruction 961
 913 of a volume of neocortex. *Cell*, 162(3):648–661, 2015. 1, 4
 914 [17] V. Kaynig, A. Vazquez-Reina, S. Knowles-Barley, 962
 915 M. Roberts, T. R. Jones, N. Kasthuri, E. Miller, J. Lichtman, 963
 916 and H. Pfister. Large-scale automatic reconstruction of 964
 917 neuronal processes from electron microscopy images. 965
 918 *Medical image analysis*, 22(1):77–88, 2015. 2
 919 [18] M. Keuper, E. Levinkov, N. Bonneel, G. Lavoué, T. Brox, 966
 920 and B. Andres. Efficient decomposition of image and mesh 967
 921 graphs by lifted multicut. In *Proceedings of the IEEE Inter- 968
 922 national Conference on Computer Vision*, pages 1751–1759, 969
 923 2015. 2, 4
 924 [19] S. Knowles-Barley, V. Kaynig, T. R. Jones, A. Wilson, 970
 925 J. Morgan, D. Lee, D. Berger, N. Kasthuri, J. W. Lichtman, 971
 926 and H. Pfister. Rhoananet pipeline: Dense automatic neural 972
 927 annotation. *arXiv preprint arXiv:1611.06973*, 2016. 1, 2
 928 [20] K. Lee, A. Zlateski, V. Ashwin, and H. S. Seung. Recur- 929
 929 sive training of 2d-3d convolutional networks for neuronal 930
 930 boundary prediction. In *Advances in Neural Information 931
 931 Processing Systems*, pages 3573–3581, 2015. 1, 2
 932 [21] A. L. Maas, A. Y. Hannun, and A. Y. Ng. Rectifier nonlin- 933
 933 earities improve neural network acoustic models. In *Proc. 934
 934 ICML*, volume 30, 2013. 4
 935 [22] M. Meila. Comparing clusterings by the variation of infor- 936
 936 mation. In *Colt*, volume 3, pages 173–187. Springer, 2003. 937
 937 6
 938 [23] Y. Nesterov. A method of solving a convex programming 939
 939 problem with convergence rate $O(1/k^2)$. 4
 940 [24] J. Nunez-Iglesias, R. Kennedy, S. M. Plaza, A. Chakraborty, 941
 941 and W. T. Katz. Graph-based active learning of agglomera- 942
 942 tion (gala): a python library to segment 2d and 3d neuroim- 943
 943 ages. *Frontiers in neuroinformatics*, 8, 2014. 1, 2, 3
 944 [25] T. Parag. What properties are desirable from an elec- 945
 945 tron microscopy segmentation algorithm. *arXiv preprint 946
 946 arXiv:1503.05430*, 2015. 2
 947 [26] T. Parag, A. Chakraborty, S. Plaza, and L. Scheffer. A 948
 948 context-aware delayed agglomeration framework for elec- 949
 949 tron microscopy segmentation. *PLOS ONE*, 10(5):1–19, 05 950
 950 2015. 2, 3, 4, 5
 951 [27] T. Parag, F. Tschopp, W. Grisaitis, S. C. Turaga, X. Zhang, 952
 952 B. Matejek, L. Kamentsky, J. W. Lichtman, and H. Pfister. 953
 953 Anisotropic em segmentation by 3d affinity learning and ag- 954
 954 glomeration. *arXiv preprint arXiv:1707.08935*, 2017. 1, 2
 955 [28] S. M. Plaza, T. Parag, G. B. Huang, D. J. Olbris, M. A. 956
 956 Saunders, and P. K. Rivlin. Annotating synapses in large 957
 957 em datasets. *arXiv preprint arXiv:1409.1801*, 2014. 6
 958 [29] D. Rolnick, Y. Meirovitch, T. Parag, H. Pfister, V. Jain, 959
 959 J. W. Lichtman, E. S. Boyden, and N. Shavit. Morpho- 960
 960 logical error detection in 3d segmentations. *arXiv preprint 961
 961 arXiv:1705.10882*, 2017. 2
 962 [30] O. Ronneberger, P. Fischer, and T. Brox. U-net: Convolu- 963
 963 tional networks for biomedical image segmentation. In *964
 964 International Conference on Medical Image Computing and 965
 965 Computer-Assisted Intervention*, pages 234–241. Springer, 966
 966 2015. 1, 2, 4
 967 [31] M. Sato, I. Bitter, M. A. Bender, A. E. Kaufman, and 968
 968 M. Nakajima. Teasar: Tree-structure extraction algorithm 969
 969 for accurate and robust skeletons. In *Computer Graphics and 970
 970 Applications, 2000. Proceedings. The Eighth Pacific Confer- 971
 971 ence on*, pages 281–449. IEEE, 2000. 3
 972 [32] P. Schlegel, M. Costa, and G. S. Jefferis. Learning from 973
 973 connectomics on the fly. *Current Opinion in Insect Science*, 974
 974 2017. 4
 975 [33] J. Shi and J. Malik. Normalized cuts and image segmen- 976
 976 tation. *IEEE Transactions on pattern analysis and machine 977
 977 intelligence*, 22(8):888–905, 2000. 2

- 972 [34] S.-y. Takemura, Y. Aso, T. Hige, A. M. Wong, Z. Lu, C. S. 1026
973 Xu, P. K. Rivlin, H. F. Hess, T. Zhao, T. Parag, S. Berg, 1027
974 G. Huang, W. T. Katz, D. J. Olbris, S. M. Plaza, L. A. 1028
975 Umayam, R. Aniceto, L.-A. Chang, S. Lauchie, and et al. 1029
976 A connectome of a learning and memory center in the adult 1030
977 drosophila brain. *eLife*, 6:e26975, 2017 Jul 18 2017. 4 1031
978 [35] S. Tatiraju and A. Mehta. Image segmentation using k-means 1032
979 clustering, em and normalized cuts. *Department of EECS*, 1033
980 1:1–7, 2008. 2 1034
981 [36] S. Turaga, K. Briggman, M. Helmstaedter, W. Denk, and 1035
982 S. Seung. Maximin affinity learning of image segmentation. 1036
983 In *Advances in Neural Information Processing Systems* 22. 1037
984 2009. 4 1038
985 [37] S. C. Turaga, J. F. Murray, V. Jain, F. Roth, M. Helmstaedter, 1039
986 K. Briggman, W. Denk, and H. S. Seung. Convolutional net- 1040
987 works can learn to generate affinity graphs for image seg- 1041
988 mentation. *Neural computation*, 22(2):511–538, 2010. 2 1042
989 [38] A. Vázquez-Reina, M. Gelbart, D. Huang, J. Lichtman, 1043
990 E. Miller, and H. Pfister. Segmentation fusion for connec- 1044
991 toomics. In *Proc. IEEE ICCV*, pages 177–184, Nov 2011. 2 1045
992 [39] N. M. Zaitoun and M. J. Aqel. Survey on image segmenta- 1046
993 tion techniques. *Procedia Computer Science*, 65:797–806, 1047
994 2015. 2 1048
995 [40] T. Zhao and S. M. Plaza. Automatic neuron type identifica- 1049
996 tion by neurite localization in the drosophila medulla. *arXiv 1050*
997 preprint arXiv:1409.1892, 2014. 3 1051
998 [41] A. Zlateski and H. S. Seung. Image segmentation by size- 1052
999 dependent single linkage clustering of a watershed basin 1053
1000 graph. *arXiv preprint arXiv:1505.00249*, 2015. 1, 2, 4 1054
1001 [42] J. Zung, I. Tartavull, and H. S. Seung. An error detec- 1055
1002 tion and correction framework for connectomics. *CoRR*, 1056
1003 abs/1708.02599, 2017. 2 1057
1004
1005
1006
1007
1008
1009
1010
1011
1012
1013
1014
1015
1016
1017
1018
1019
1020
1021
1022
1023
1024
1025